Two-dimensional growth, anisotropic polaron transport and magnetic phase segregation in epitaxial $Nd_{0.52}Sr_{0.48}MnO_3$ films

V.G. Prokhorov and G.G. Kaminsky

Institute of Metal Physics, NASU, Kiev 03142, Ukraine
E-mail: pvg@imp.kiev.ua

J.M. Kim, T.W. Eom, J.S. Park, and Y.P. Lee

q-Psi and Department of Physics, Hanyang University, Seoul 133-791, Korea

V.L. Svetchnikov

National Center for HREM, TU Delft, 2628AL, The Netherlands

G.G. Levtchenko, A.V. Paschenko, Yu.V. Medvedev, Yu.M. Nikolaenko, G.V. Bukin, and V.A. Khokhlov

Donetsk Institute for Physics and Technology, NASU, Donetsk 83114, Ukraine

$Nd_{0.52}Sr_{0.48}MnO_3$ films have been prepared by dc magnetron sputtering on $LaAlO_3$ (001) and $SrTiO_3$ (011) single-crystalline substrates with an additional annealing for the lattice strain relaxation. Even though that the $Nd_{0.52}Sr_{0.48}MnO_3$ films were deposited simultaneously on different substrates at the same deposition rate they differ in the thickness by $\simeq \sqrt{2}$. The observed difference in the thickness is explained by the two-dimensional (layer-by-layer) growth of film rather than a difference in the growth rate, controlled by the crystal orientation of substrate. The analysis of the optical and transport properties reveals that the observed anisotropy in the polaron motion is governed by a strong anisotropy of the trapping energy rather than the polaron formation one. It was shown that the deposited $Nd_{0.52}Sr_{0.48}MnO_3$ films manifest a magnetic behavior typical for two-phases magnetic systems and must be considered as an assembly of interacting magnetic clusters.

1. Introduction

Hole-doped manganites $L_{1-x}A_xMnO_3$, where L and A are a trivalent lanthanide ion and a divalent alkaline-earth ion, respectively, have attracted considerable attention due to their interesting fundamental science, connected with colossal magnetoresistance (CMR), and potential for applications [1]. However, practical employment of these potential applications requires the solutions of basic material problems coupled to the structure–property relationships. The doped manganite perovskites exhibit a strong correlation between their lattice structure and the magneto-transport properties, and this phenomenon becomes more important in the thin films [2–5]. Let us take $Nd_{0.52}Sr_{0.48}MnO_3$ thin films as an example. According to the phase diagram [6], $Nd_{1-x}Sr_xMnO_3$ is a typical system whose ground state varies from a ferromagnetic (FM) metal to an A-type antiferromagnetic (AFM) metal when the Sr doping crosses

0.5. In addition, a charge-ordered (CO) phase with the so-called CE-type AFM structure is formed in a very narrow doping range near $x \approx 0.5$. At the same time, the ground state of this compound is drastically dependent on the degree of crystallinity, the lattice strain, the chemical homogeneity, and the clustering of microstructure, which are controlled by the fabrication technique. Thus the CO state can be stabilized by a long-ranged lattice strain, which is accumulated during the film deposition [7,8]. The CO CE-type AFM state can be suppressed by increasing the film thickness [9], with a high hydrostatic pressure [10,11], by decreasing the grain size in polycrystalline samples [12,13], and by applying an electric field [14]. Therefore, the film crystallinity, the microstructure, and the epitaxial relationship to substrate need to be fully controlled in order to obtain the high-quality single or multilayer epitaxial films for specific applications.

In this paper we report the experimental results for $Nd_{0.52}Sr_{0.48}MnO_3$ (NSMO) films deposited on $LaAlO_3$ (001) and $SrTiO_3$ (011) single-crystalline substrates. The observed evidence for two-dimensional growth of the film and the significant difference in physical properties, governed by the crystal-lattice anisotropy, are discussed in detail.

2. Experimental techniques

The films were prepared by dc magnetron sputtering at a substrate temperature of 650 °C [15]. To avoid the influence of lattice strain, accumulated during deposition, the all films were annealed at 900 °C for 2 h in air. The $\theta-2\theta$ x-ray diffraction (XRD) patterns were obtained using a Rigaku diffractometer with Cu K_α radiation. The lattice parameters evaluated directly from the XRD data were plotted against $\cos^2\theta/\sin\theta$. From the intercept of the extrapolated straight line to $\cos^2\theta/\sin\theta = 0$, a more precise lattice parameter was obtained. The high-resolution electron-microscopy (HREM) study was carried out using a Philips CM300UT-FEG microscope with a field emission gun operated at 300 kV. The point resolution of the microscope was in the order of 0.12 nm. The cross-sectional specimens were prepared by the standard techniques using mechanical polishing followed by ion-beam milling at a grazing incidence. All microstructure measurements were carried out at room temperature. The resistance measurements were made by the four-probe method in a temperature range of 4.2–300 K and a magnetic field up to 5 T. The field-cooled (FC) and the zero-field-cooled (ZFC) magnetization curves were taken with a Quantum Design SQUID magnetometer for the in-plane magnetic field orientation. The magnetization curves obtained for the bare substrates were extracted from the raw experimental curves. The optical-density (OD) spectra were obtained using a PGS-2 spectrograph from Carl Zeiss CmbH.

3. Microstructure and two-dimensional growth of films

Figure 1 presents the $\theta-2\theta$ XRD scans for the films, which were simultaneously deposited on $LaAlO_3$ (LAO) and $SrTiO_3$ (STO) substrates at the same conditions. Only the fundamental Bragg peaks of high intensity for the film (F) and the substrate (S) are observed, indicating that the deposition results in a highly oriented crystal structure. It is confirmed by analysis of the transmission contrast of the HREM images. At the same time the cross-sectional low-magnification HREM images, represented by the insets in Fig. 1, manifest that the obtained films have significantly different thicknesses ($d = 85$ and 60 nm for the film deposited on LAO and STO, respectively), in spite of the same deposition rate. Therefore, one can concede that the growth rates of film are different on the LAO (001) and the STO (011) substrates. This is a fully expected result, taking into account that the growth rate for cubic crystals along the [100] orientation, as a rule, is quite higher than that along [110]. It was shown recently that the growth-speed ratio s_{100}/s_{110} varies in a range of 1.2–1.8 for face-centered cubic structures [16]. In our case, assuming that the growth speed is equal to be d/t, where t is deposition time, $s_{100}/s_{110} \simeq 1.42$, which is well coincident with the theoretical prediction. However, other things also affect the thickness of film deposited on a single-crystalline substrate.

Figure 2 shows the cross-sectional high-magnification HREM images taken from the [010] zone axis for the films, deposited on LAO (*a*) and STO (*b*), including the film/substrate interfaces. It is seen that the both films manifest the atomically clean and sharp interface without an amorphous intermediate layer or precipitations. The epitax-
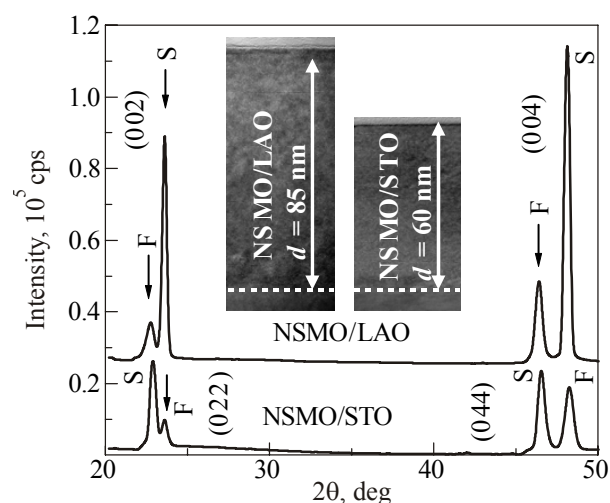

Fig. 1. XRD scans for the NSMO/LAO and NSMO/STO films. F and S indicate the fundamental Bragg peaks for the film and the substrate, respectively. Insets are the low-magnification cross-sectional HREM images taken at room temperature for the corresponding films. It is seen that the films have different thicknesses.
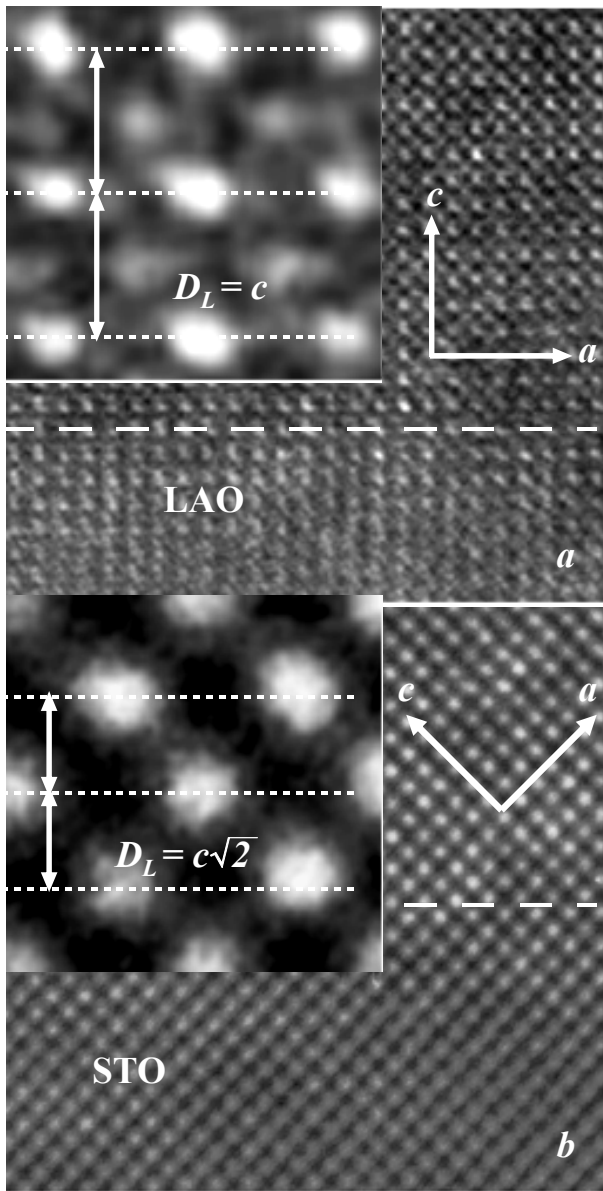
Fig. 2. High-magnification cross-sectional HREM images taken at room temperature for NSMO/LAO (*a*) and NSMO/STO (*b*) films. Dashed lines indicate the interface between film and substrate. *c* and *a* are the axes of crystal lattice. Insets show the atomic structure of films in ditail. D_L denotes the atomic layer thickness.

ial relationships for film and substrate are determined to be $[001]_{\mathrm{NSMO}} \parallel [001]_{\mathrm{LAO}}$ and $[011]_{\mathrm{NSMO}} \parallel [011]_{\mathrm{STO}}$. Insets in Fig. 2 display that the distances between atomic rows (the atomic layer thickness D_L), which are formed onto the substrate surface during deposition, are significantly different: $D_L = c$ and $c/\sqrt{2}$ for the NSMO/LAO and the NSMO/STO films, respectively, where c is the out-of-plane lattice parameter for the cubic symmetry. This fact can elucidate the growth mechanism.

Three kinds of the growth mechanism are typical for thin films. There are the Volmer–Weber (island) mode, the Frank–van der Merwe (layer) mode, and the intermediate

Stranski–Krastanov (layer-plus-island) mode [17]. The well-defined atomic layered structure of the films (see Fig. 2) allows us to suggest that only last two mechanisms can be realized in our case, because both of them assume the layer-by-layer growth of film. Taking into account that the layer-plus-island mode is preferred with respect to the layer one, owing to the adsorption-energy competition [17], one can conclude that the investigated films are grown through the Stranski–Krastanov mechanism. In this case the film thickness can be expressed by the product of atomic-layer number (n_L) and layer thickness: $d = n_L D_L$. Even assuming that the number of layers is equal for both films, the thickness ratio for the NSMO/LAO and the NSMO/STO films is changed, according to the difference in the layer thickness: $D_L^{\mathrm{LAO}} / D_L^{\mathrm{STO}} \simeq \sqrt{2}$. Therefore, it is understood that the observed same difference in the grown thickness of films is provided by the special two-dimensional (layer-by-layer) film growth.

4. Experimental results

Figure 3,*a* shows the OD spectra for the NSMO/LAO and the NSMO/STO films with d = 85 and 60 nm, respectively, taken at room temperature. The OD spectra obtained for the bare substrates were extracted from the raw experimental curves. It is seen that the first difference in the optical properties between NSMO/STO and NSMO/LAO films is connected with the transmission (T) value, which is higher by nearly an order for the NSMO film, deposited on the LAO (001) substrate. Similar peculiarity in the OD spectra for half-doped NSMO films was observed earlier at low temperatures, and explained by the strong anisotropy in the orbital ordering [7]. On the other hand, the low-energy region in the optical spectra for manganites is identified as an incoherent background which involves the strong Jahn–Teller interactions with the polaron terms, and results in the charge-transfer excitations from the oxygen 2*p*-band states to the bands involving the manganese e_g states near 3 eV [18]. Furthermore, the crystal-field splitting governed by the Jahn–Teller effect would split the energies of the charge-transfer excitations, and form the fine structure of the central peak (indicated by arrows in Fig. 3,*a*). The energy difference turns out to be charge-transfer $\simeq$ 76 and 73 meV, for NSMO/STO and NSMO/LAO, respectively. These values are very close to the polaronic gap, which is typical for this compound in a temperature range above the metal–insulator (MI) transition [19].

Figure 3,*b* shows the temperature dependance of resistance, $R(T)$ without (open symbols) and with (solid symbols) an applied magnetic field of 5 T, for the same films. Analysis of the experimental $R(T)$ curves in the framework of the small-polaron motion model [20], $R(T) \sim T \exp(E_A/k_B T)$, where E_A is an activation energy and k_B is the Boltzmann constant, reveals that $E_A =$
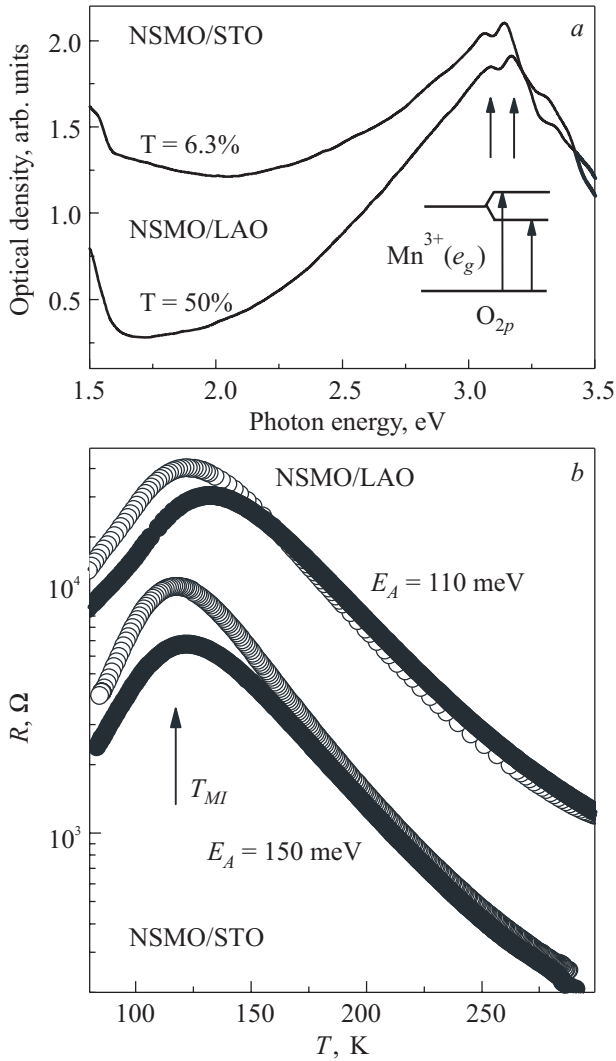
Fig. 3. (*a*) Optical-density spectra for NSMO/LAO and NSMO/STO films, taken at room temperature. T is the transmission value. Arrows indicate the fine structure of a charge-transfer peak, governed by the e_g-level splitting. (*b*) Temperature dependence of the resistance for NSMO/LAO and NSMO/STO films, without (open symbols) and with (solid symbols) an applied magnetic field of 5 T. Arrow indicates the MI transition temperature. E_A is activation energy, obtained in framework of the small polaron model.

Fig. 4. Temperature dependence of the in-plane FC (solid symbols) and the ZFC (open symbols) magnetic moments for the NSMO/STO films with thickness $d = 240$ (*a*), 120 (*b*) and 60 (*c*) nm at different applied magnetic fields.

= 150 and 110 meV, for NSMO/STO and NSMO/LAO, respectively.

Figure 4 shows the in-plane FC (solid symbols) and the ZFC (open symbols) temperature dependences of the magnetic moment, $M(T)$, for the NSMO/STO films with thickness $d = 240$ (*a*), 120 (*b*) and 60 (*c*) nm at different applied magnetic fields. The ZFC and FC $M(T)$ curves were obtained at the increasing temperature after the film cooling without and with an external magnetic field, respectively. All films manifest the FM transition with decreasing temperature at the Curie temperature $T_C \simeq 220$ K, which is very close to the published data for this compound [6,21]. At the same time, the films manifest the

well-defined ZFC/FC $M(T)$ splitting (even for the high applied magnetic fields), which is typical for the magnetic multiphase [cluster-glass or superparamagnetic (SPM)] systems. A coexistence of the small-size FM and AFM clusters at low temperature has already been observed in the similar compounds [12,22,23]. It was shown, that the AFM clusters occur due to a crystal-lattice transition from orthorhombic to monoclinic phase at $T \le T_N$ with the formation of a twin domain structure [24]. The Néel temperature, T_N, which was extracted from the reduced magnetic moment $M_{FC}/M_{ZFC}(T)$ dependence (not shown) [25], turns out to be also the same for all films, $T_N \simeq 150$ K.
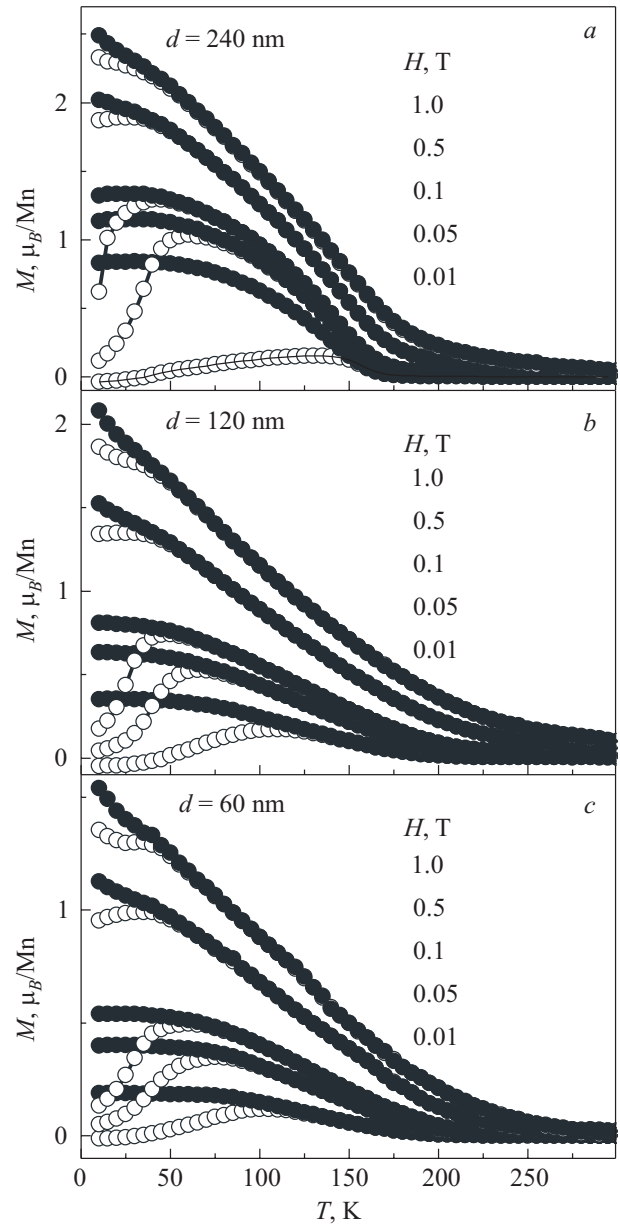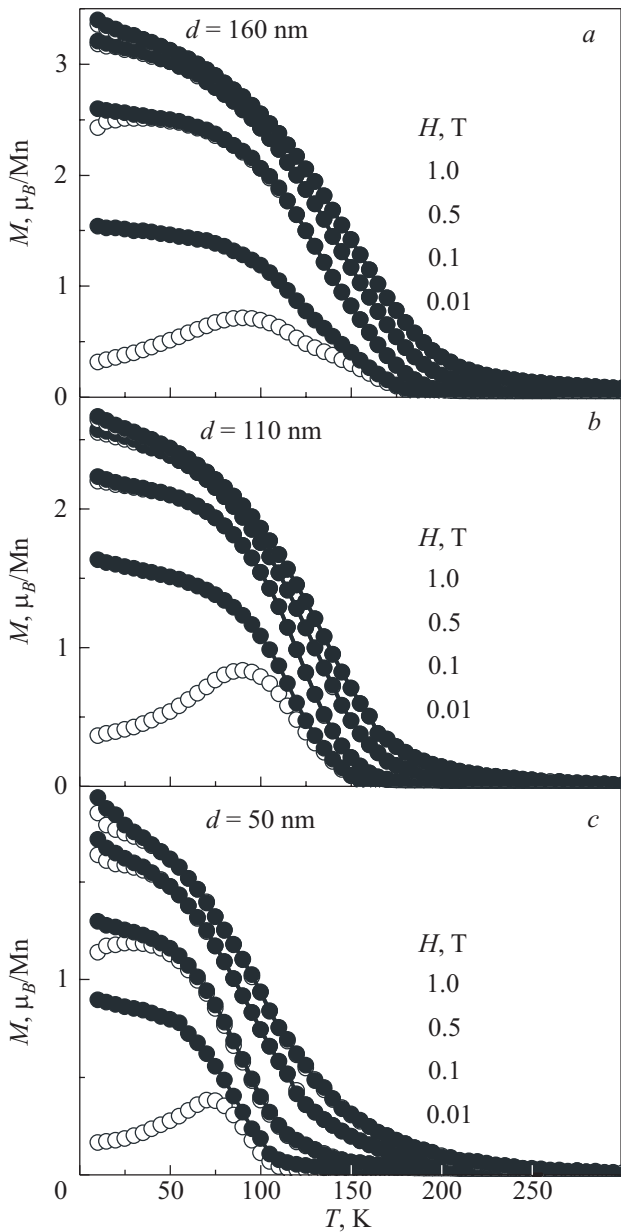
144

Fig. 5. Temperature dependence of the in-plane FC (solid symbols) and the ZFC (open symbols) magnetic moments for the NSMO/LAO films with thickness $d = 160$ (*a*), 110 (*b*) and 50 (*c*) nm at different applied magnetic fields.

Fig. 6. Magnetic field dependences of the in-plane magnetic moment for (*a*) NSMO/LAO with $d = 50$ (*1*), 110 (*2*) and 160 (*3*) nm, and (*b*) for NSMO/STO with $d = 60$ (*1*), 120 (*2*) and 240 (*3*) nm, measured at 10 K. Lines are guides to the eyes.

Figure 5 presents the similar $M(T)$ dependences for the NSMO/LAO films with thickness $d = 160$ (*a*), 110 (*b*) and 50 (*c*) nm at different applied magnetic fields. These films manifest a significant thickness dependence of the Curie temperature and a minor FC/ZFC $M(T)$ splitting (excepting the thinner film), in contrast to the NSMO/STO ones. At the same time, the Néel temperature is almost identical for these films, $T_N \simeq 125$ K. Analysis of the $M(T)$ curves reveals that $T_C \simeq 220$, 180 and 115 K for NSMO/LAO with $d = 160$, 110 and 50 nm, respectively.

Figure 6 displays the in-plane hysteresis loops, $M(H)$, taken at 10 K for the NSMO/LAO (*a*) and NSMO/STO (*b*)
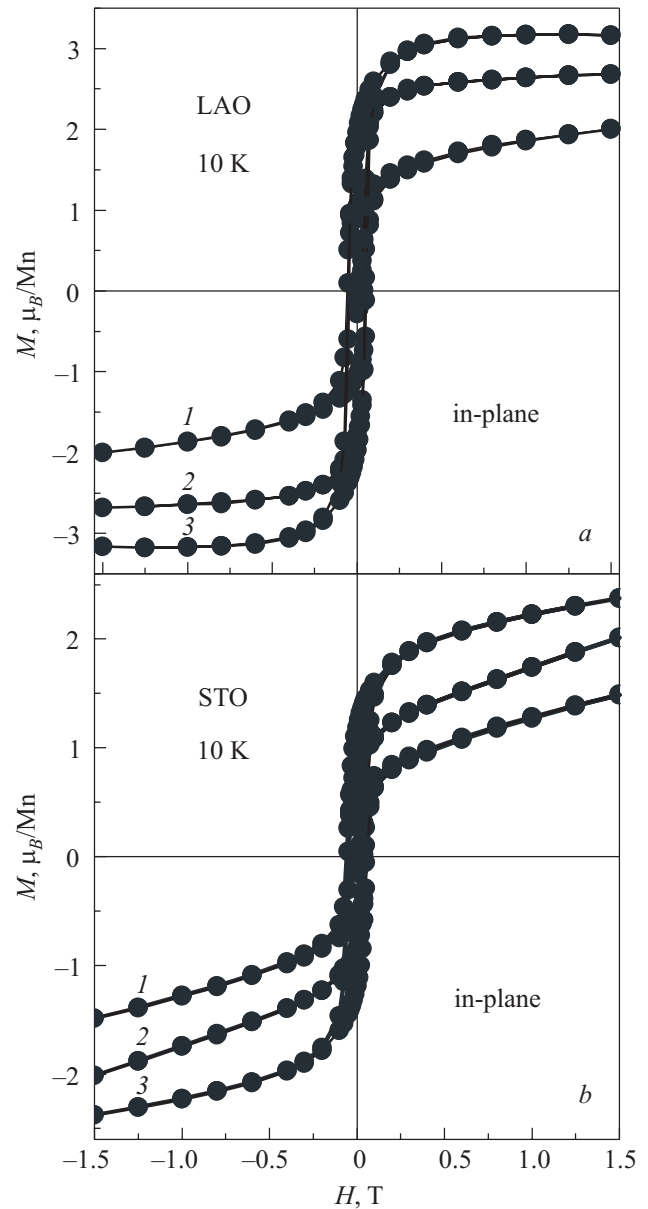
films with different thickness. All film were measured in the ZFC regime. It is seen that the NSMO/LAO films demonstrate the saturation magnetic moment, M_s, greatly higher than the NSMO/STO ones. Moreover, the $M(H)$ curves for the NSMO/STO films are unsaturated up to the highest magnetic field and demonstrate the linear increase with increasing magnetic field that implies a presence of the AFM phase. At the same time, the similar unsaturated hysteresis loop is observed for NSMO/LAO with $d \simeq 50$ nm, as well.

The main magnetic characteristics of the films are summarized in Table 1.

Table 1. Magnetic characteristics for the investigated films

Samples	Thickness d, nm	Curie point T_C, K	Néel point T_N, K	Saturation magnetic moment M_s, μ_B/Mn	Remanence magnetic moment M_r, μ_B/Mn	Coercive field H_c, Oe
NSMO/STO	60	220	150	0.88	0.55	580
NSMO/STO	120	220	150	1.26	0.85	500
NSMO/STO	240	220	150	1.92	1.21	450
NSMO/LAO	50	115	125	1.71	1.11	600
NSMO/LAO	110	180	125	2.73	1.79	550
NSMO/LAO	160	220	125	3.45	2.03	500

5. Discussion

Let us consider the observed anisotropic origin of polaron state in these films more in detail. In the adiabatic limit the activation energy for the small-lattice-polaron (Holstein) motion involves two terms, $E_A = E_g/2 + W_H$, where E_g is the so-called trapping energy or the energy difference between the lattice distortion with and without a hole and W_H is the polaron formation energy [20]. The polaron formation energy in our case can be attributed to the energy splitting of the charge-transfer central peak (see inset in Fig. 3,a), which is interpreted as a polaronic gap, $W_H = \Delta_g$, and is almost coincident for the NSMO/STO and NSMO/LAO films. At the same time the difference between E_A and W_H is greatly differ for these films: 74 and 37 meV for NSMO/STO and NSMO/LAO, respectively. Consequently, the observed anisotropy of the polaron motion is governed by a strong anisotropy of the trapping energy, E_g, rather than the polaron formation one, W_H.

Analysis of the $M(T)$ dependencies for investigated films (see Figs. 4 and 5) reveals that T_C almost does not depend on the thickness for NSMO/STO while is very sensitive to that for NSMO/LAO (see Table 1). This phenomenon is mainly controlled by the lattice strain, accumulated due to the epitaxial growth of the films, which greatly affects a formation of the spin-ordered state. Let us analyze the obtained results on the basis of the Millis model [26]. For a weak lattice strain ε and a cubic symmetry T_C can be expressed as

$$T_C(\varepsilon) = T_{C0}\left(1 - \alpha\varepsilon_B - \frac{1}{2}\Delta\varepsilon_{JT}^2\right), \qquad (1)$$

where $T_{C0} = T_C(\varepsilon = 0)$, $\alpha = (1/T_{C0})(dT_C/d\varepsilon_B)$, and $\Delta = (1/T_{C0})(d^2T_C/d\varepsilon_{JT}^2)$. The magnitudes of α and Δ represent the relative weights for the symmetry-conserving bulk strain ε_B and the symmetry-breaking Jahn–Teller strain ε_{JT}, respectively. According to the model, $\alpha \simeq 10$ for a reasonable electron–phonon coupling ($0.5 \leq \lambda \leq 1$) in this compound, where λ is the electron-phonon-interaction

constant, and $\Delta \simeq 5000$. The bulk strain $\varepsilon_B = (2\varepsilon_{100} + \varepsilon_{001})$ and the Jahn–Teller strain $\varepsilon_{JT} = \sqrt{2/3}(\varepsilon_{001} - \varepsilon_{100})$, where $\varepsilon_{100} = (a_{\text{bulk}} - a_{\text{film}})/a_{\text{bulk}}$ and $\varepsilon_{001} = (c_{\text{bulk}} - c_{\text{film}})/c_{\text{bulk}}$ are in-plane and out-of-plane lattice strains. For example, let us consider the change of T_C, which is predicted by the model, for the NSMO/STO and NSMO/LAO films with the maximum and minimum thickness. The analysis of XRD and HREM data reveals that in-plane and out-of-plane lattice parameters for NSMO/STO correspond to $a \simeq 0.386$ and 0.387 nm, $c \simeq 0.3823$ and 0.381 nm for $d \simeq 240$ and 60 nm, respectively. Similar for NSMO/LAO: $a \simeq 0.384$ and 0.379 nm, $c \simeq 0.388$ and 0.394 nm for $d \simeq 160$ and 50 nm, respectively. The estimated values of ε_{100} and ε_{001} manifest that the NSMO/STO films have biaxial tensile in-plane and compressive out-of-plane lattice strains while the NSMO/LAO ones are exposed to compressive in-plane and tensile out-of-plane strains. Notice that the obtained result is typical for manganite films, deposited on the STO and LAO substrates [27,28]. Using the Curie point and the lattice parameters of thick films as a "bulk", we estimated the corresponding T_C values for NSMO/STO ($d \simeq 60$ nm) and NSMO/LAO ($d \simeq 50$ nm) as 211 and 118 K, respectively, which are excellently agree with the experimental data (see Table 1).

Therefore, one can conclude that the observed thickness dependence of the Curie temperature in the $Nd_{0.52}Sr_{0.48}MnO_3$ films, deposited on $SrTiO_3$ (011) and $LaAlO_3$ (001) single-crystalline substrates is controlled by sign and intensity of accumulated lattice strains.

At the same time, according to the magnetic phase diagram, $Nd_{0.52}Sr_{0.48}MnO_3$ undergoes the AFM transition (CE-type) at $T_N \leq 150$ K. The magnetic measurements (see Table 1) testify that the Néel temperature does not depend on thickness while is slight smaller for the NSMO/LAO films. Similar to the Curie point, the observed slight difference in T_N between NSMO/STO and NSMO/LAO can be explained by the different lattice-strain intensity in these films as well.

Figure 6 manifests that the NSMO/LAO films have a larger saturation magnetic moment (M_s) and a remanence (M_r) than the NSMO/STO ones. Moreover, M_s and M_r decrease with decreasing thickness for both kinds of the films. The saturation magnetic moment per unit cell determines, as a rule, the volume of FM phase in a sample. For NSMO/LAO with $d \simeq 160$ nm $M_s \simeq 3.45$ μ_B/Mn while for NSMO/STO with $d \simeq 240$ nm $M_s \simeq 2$ μ_B/Mn. In addition, the $M(H)$ hysteresis loops for all NSMO/STO films (together with thinnest NSMO/LAO) remain unsaturated up to highest applied magnetic field and demonstrate the linear increase of magnetic moment with a rise of H, which is typical for the AFM phase. Therefore, the $Nd_{0.52}Sr_{0.48}MnO_3$ films can be treated as a two-phase magnetic systems, the magnetic properties of which are controlled by the competition between ferromagnetic-double exchange and antiferromagnetic-superexchange. On

the other hand, the hole-doped perovskite manganites belong to the strongly correlated systems and have a tendency toward the phase separation, including the magnetic one [1]. Therefore, both the magnetic phases are segregated on the FM and AFM clusters and are coexisted at $T \leq T_N$ [22,29].

The main evidence for a magnetic phase separation (or a magnetic clustering) is the ZFC/FC $M(T)$ splitting, which is observed for all NSMO/STO films and for NSMO/LAO with $d \simeq 50$ nm in a wide range of applied magnetic fields (see Figs. 4 and 5). This phenomenon interprets as an origin of the glassy magnetic behavior and the phase segregated state is treated as cluster-glass or spin-glass-like phase [30].

Figure 7,*a* shows the magnetic field dependencies of the splitting point between ZFC–FC $M(T)$ curves, $T^*(H)$, for NSMO/STO ($d \simeq 60$, 120 and 240 nm) and NSMO/LAO ($d \simeq 50$ nm). All films manifest a strong and a similar $T^*(H)$ dependence proportional to $\sim 1/H$.

According to the classical spin-glass model, the $T^*(H)$ behavior is described by the Almeida–Thouless ZFC/FC $M(T)$ irreversibility line [31]:

$$T^*(H) = T^*(0) \left[1 - \left(\frac{3}{4} \frac{H^2}{J^2} \right)^{1/3} \right], \qquad (2)$$

where J is the exchange integral, which can be described by $J = 3k_B T_C / [2zS(S+1)]$, where T_C is the Curie temperature, $z = 6$ is the number of nearest neighbor atoms (because we consider the cubic unit cell) and $S = 1.74$ is the spin value (as an average of $S_1 = 2$ and $S_2 = 3/2$ which correspond to the Mn^{4+} and the Mn^{3+} ions, respectively). Figure 7,*a* demonstrates the Almeida–Thouless curve (ATL), which was obtained without any fitting parameters, using experimental values for the Curie point (220 K) and the saturation magnetic moment for complete FM state ($\simeq 3.45$ μ_B/Mn). It is seen that theoretical curve demonstrates a more weak $T^*(H)$ dependence in comparison with the experimental data. An alternative cluster-glass (or droplet) model [32], which involves the field dependence of a magnetic correlation length, predicts the strong rise of T^* with increasing magnetic field, which is in contrast with our results [30].

On the other hand, the magnetic phase-separated state can be considered as an ensemble of the superparamagnetic (SPM) particles. In this case T^* identifies with a blocking temperature (T_B), given by $k_B T_B \simeq KV_{SPM}$ [33,34], above which the magnetic moments of the SPM particles move freely owing to thermal fluctuations while they are transformed into the blocked state at $T \leq T_B$. Here KV_{SPM} is the energy barrier between two directions of the magnetic moment in a single SPM particle — along and against an applied magnetic field, and K is the magnetic anisotropy constant. For noninteracting SPM particles the $T_B(H)$ dependence expressed as [35,36]

$$T_B(H) = T_B(0) \left(1 - \frac{H}{H_0} \right)^2, \qquad (3)$$

where $T_B(0)$ is the blocking temperature without magnetic field and $H_0 = 2K / \mu_0 M_s$. The theoretical curve, denoted as N-SPM, was calculated using the experimental data, $K \simeq 8.4 \cdot 10^4$ J·m^{-3} (for the $Nd_{0.5}Sr_{0.5}MnO_3$ film) [3,4] and $M_s \simeq 3.45 \mu_B$/Mn. However, it is seen that, similar to the spin-glass-like model, a significant disagreement between the experimental and theoretical $T_B(H)$ dependencies is observed as well.

Lately the model of an interacting superparamagnetic (I-SPM) phase has been employed for the analysis of SPM materials, which is taken into account the strong dipolar
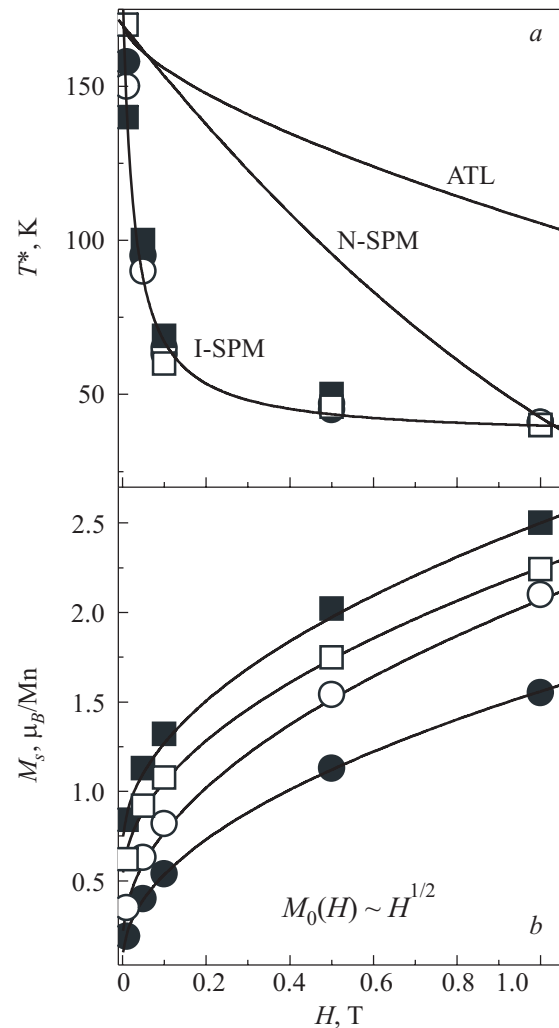

Fig. 7. (*a*) Magnetic field dependencies of the splitting point between ZFC–FC $M(T)$ curves, $T^*(H)$, for the NSMO/STO [$d \simeq 60$ (solid squares), 120 (open circles) and 240 nm (solid circles)] and the NSMO/LAO [$d \simeq 50$ nm (open squares)] films. Solid lines are theoretical curves predicted by the spin-glass (ATL), the noninteracting superparamagnets (N-SPM) and the interacting superparamagnets (I-SPM) models. (*b*) Magnetic field dependencies of the saturation magnetic moment extracted from the FC $M(T)$ experimental curves for the same films. Solid lines are the fitting curves described in text.

interaction between SPM clusters [4,37–40]. Apart from the direct numerical simulations, the dipolar interaction is introduced by properly modifying the argument of Langevin function for the noninteracting SPM particles: $\mu_{eff}H/k_BT \to \mu H/k_B(T+T_D)$, where $T_D = \alpha M_0^2/k_B N$ is the so-called "dipolar temperature", α is a constant of the order of unity, N is the Mn-ions number per unit volume, and M_0 is a magnetic moment at $T = 0$ K, taken from the $M(T)$ experimental curves at different applied magnetic field. Taking into account that $\mu_{eff} \sim V_{SPM} \sim T_B$ and $N = 1$ in our case, one can written

$$T_B(H) = T_B(0)\frac{1}{[1+\alpha M_0^2/k_BT]}. \quad (4)$$

Figure 7,*b* shows that the magnetic field dependencies of M_0 for the NSMO/STO films can be excellently fitted by the universal function: $M_0(H) = AH^{1/2}$, where A is varied from 1.9 to 1.5 $\mu_B \cdot T^{-1/2}$ with the decreasing thickness. Therefore, the Eq. (4) can be modified as $T_B(H) = T_B(0)/(1+\beta H)$, where $\beta = \alpha A^2/k_BT$. Figure 7,*a* shows that the theoretical curve, denoted as I-SPM, with the fitting parameters of $T_B(0) = 140$ K and $\beta = 35$ T^{-1}, is excellently coincident with the experimental one.

Therefore, the NSMO/STO films (and thinnest NSMO/LAO) can be treated as the interacting SPM systems rather than the classical spin glasses or the Langevin-like SPMs. At the same time the ZFC/FC $M(T)$ splitting almost does not recognize in the thick NSMO/LAO films (see Figs. 5,*a* and *b*). It is explained by a large volume of the FM phase in the films, which is confirmed by the large M_s values per unit cell (see Table 1). In this case the concentration of FM phase exceeds a percolating threshold value of the infinite FM cluster and the SPM-like effects can not observed.

6. Conclusions

We have performed the microstructure, the optical, the transport, and the magnetic measurements of the $Nd_{0.52}Sr_{0.48}MnO_3$ films prepared by dc magnetron sputtering on LaAlO$_3$ (001) and SrTiO$_3$ (011) single-crystalline substrates with an additional annealing for the lattice strain relaxation. The main results can be summarized as follows.

(1) The $\theta-2\theta$ XRD scans and the HREM images reveal that the NSMO/LAO and NSMO/STO films have a perfect microstructure and a highly oriented crystal structure with epitaxial relationships of $[001]_{NSMO}\|[001]_{LAO}$ and $[011]_{NSMO}\|[011]_{STO}$, respectively. On the other hand, even though the $Nd_{0.52}Sr_{0.48}MnO_3$ films were deposited simultaneously on different substrates at the same deposition rate, they differ in the thickness by $\simeq \sqrt{2}$. The observed difference is explained by the two-dimensional (layer-by-layer) film growth rather than a difference in the growth rate, controlled by the crystal orientation of substrate.

(2) The optical-density spectra manifest that the transmission value is higher by nearly an order for the NSMO/LAO film than that is observed for the NSMO/STO one. It is explained by an anisotropic origin of the Jahn–Teller interactions which leads to anisotropy of polaron state in this compound. Moreover, the observed slight splitting of the central peak, corresponding to the charge-transfer excitations from the oxygen 2*p*-band states to the bands involving the manganese e_g states near 3 eV, testifies that the polaronic gap of $\simeq 76$ and 73 meV, for NSMO/STO and NSMO/LAO, respectively, is formed in the films.

(3) The $R(T)$ dependencies, measured in temperature range above the MI transition, demonstrate a thermally activated behavior and can be described in the framework of a small-polaron motion model with an activation energy $E_A = 150$ and 110 meV, for NSMO/STO and NSMO/LAO, respectively. Taking into account that the polaronic gap, extracted from the OD spectra, is almost coincident for both kinds of the films, one can conclude that the observed anisotropy in the polaron motion is governed by a strong anisotropy of the trapping energy rather than the polaron formation one.

(4) It was shown that the observed thickness dependence of the Curie temperature in the $Nd_{0.52}Sr_{0.48}MnO_3$ films, deposited on SrTiO$_3$ (011) and LaAlO$_3$ (001) substrates, is controlled by the sign and intensity of accumulated lattice strains.

(5) Analysis of the magnetic properties shown that the $Nd_{0.52}Sr_{0.48}MnO_3$ films can be treated as a two-phase magnetic systems, the magnetic properties of which are controlled by the competition between ferromagnetic-double exchange and antiferromagnetic-superexchange. The magnetic phase segregation on the FM and AFM clusters, which are coexisted at $T \le T_N$, is confirmed by a splitting of the ZFC/FC $M(T)$ curves, measured at different applied magnetic fields. In contrast to a bulk material [22] and a half-doped thin film [7] the AFM phase, in our case, arises from the precursory paramagnetic state rather than from the formed FM one. At the same time, the SPM-like clustering state is recognized when a concentration of the FM phase does not exceed a percolating threshold value. The observed tendency of the (011)-oriented films to the phase separation is explained by a smaller volume of the FM phase in comparison to the (001)-oriented ones.

(6) A comprehensive analysis of the spin-glass-like and the SPM approaches reveals that the deposited $Nd_{0.52}Sr_{0.48}MnO_3$ films must be considered as an assembly of interacting magnetic clusters, quite similar to the SPM particles with dipolar interaction, at least from a magnetic point view.

1. For a review, see *Colossal Magnetoresistance, Charge Ordering and Related Properties of Manganese Oxides*, C.N.R. Rao and B. Raveau (eds.), World Scientific, Singapore (1998); *Colossal Magnetoresistance Oxides*, Y. Tokura (ed.), Gordon and Breach, London (1999); E. Dagotto, T. Hotta, and A. Moreo, *Phys. Rep.* **344**, 1 (2001).

2. F. Tsui, M.C. Smoak, T.K. Nath, and C.B. Eom, *Appl. Phys. Lett.* **76**, 2421 (2000).

3. V.G. Prokhorov, G.G. Kaminsky, V.A. Komashko, Y.P. Lee, S.Y. Park, Y.H. Hyun, J.B. Kim, J.S. Park, V.L. Svetchnikov, V.P. Pashchenko, and V.A. Khokhlov, *Fiz. Nizk. Temp.* **33**, 889 (2007) [*Low Temp. Phys.* **33**, 678 (2007)].

4. V.G. Prokhorov, Y.H. Hyun, J.S. Park, J.B. Kim, G.H. Kim, Y.S. Lee, Y.P. Lee, and V.L. Svetchnikov, *J. Appl. Phys.* **104**, 103901 (2008).

5. Y.H. Hyun, S.Y. Park, Y.P. Lee, V.G. Prokhorov, and V.L. Svetchnikov, *Appl. Phys. Lett.* **91**, 262505 (2007).

6. R. Kajimoto, H. Yoshizawa, H. Kawano, H. Kuwahara, Y. Tokura, K. Ohoyama, and M. Ohashi, *Phys. Rev.* **B60**, 6506 (1999).

7. Y. Ogimoto, M. Nakamura, N. Takubo, H. Tamaru, M. Izumi, and K. Miyano, *Phys. Rev.* **B71**, 060403 (2005).

8. M.J. Calderyn, A.J. Millis, and K.H. Ahn, *Phys. Rev.* **B68**, 100401 (2003).

9. Q. Qian, T.A. Tyson, C.-C. Kao, W. Prellier, J. Bai, A. Biswas, and R.L. Greene, *Phys. Rev.* **B63**, 224424 (2001).

10. C. Cui, T.A. Tyson, Z. Chen, and Z. Zhong, *Phys. Rev.* **B68**, 214417 (2003).

11. R.C. Yu, J. Tang, L.D. Yao, A. Matsushita, Y. Yu, F.Y. Li, and C.Q. Jin, *J. Appl. Phys.* **97**, 083910 (2005).

12. P. Levy, F. Parisi, G. Polla, D. Vega, G. Leyva, H. Lanza, R.S. Freitas, and L. Ghivelder, *Phys. Rev.* **B62**, 6437 (2000).

13. S. Dong, F. Gao, Z.Q. Wang, J.M. Liu, and Z.F. Ren, *Appl. Phys. Lett.* **90**, 082508 (2007).

14. V. Ponnambalam, S. Parashar, A.R. Raju, and C.N.R. Rao, *Appl. Phys. Lett.* **74**, 206 (1999).

15. V.N. Varyukhin, Yu.V. Medvedev, Yu.M. Nikolaenko, A.B. Mukhin, B.V. Belyaev, V.A. Gritskikh, I.V. Zhikharev, S.V. Kara-Murza, N.V. Korchikova, and A.A. Tikhii, *Technical Phys. Lett.* **35**, 937 (2009).

16. G. Tegze, L. Gránásy, G.I. Tyth, F. Podmaniczky, A. Jaatinen, T. Ala-Nissila, and T. Pusztai, *Phys. Rev. Lett.* **103**, 035702 (2009).

17. J.A. Venables, G.D.T. Spiller, and M. Hanbücken, *Rep. Prog. Phys.* **47**, 399 (1984).

18. A. Rusydi, R. Rauer, G. Neuber, M. Bastjan, I. Mahns, S. Müller, P. Saichu, B. Schulz, S.G. Singer, A.I. Lichtenstein, D. Qi, X. Gao, X. Yu, A.T.S. Wee, G. Stryganyuk, K. Dörr, G.A. Sawatzky, S.L. Cooper, and M. Rübhausen, *Phys. Rev.* **B78**, 125110 (2008).

19. M. Quijada, J. Černe, J.R. Simpson, H.D. Drew, K.H. Ahn, A.J. Millis, R. Shreekala, R. Ramesh, M. Rajeswari, and T. Venkatesan, *Phys. Rev.* **B58**, 16093 (1998).

20. E. Iguchi, K. Ueda, and W. Jung, *Phys. Rev.* **B54**, 17431 (1996).

21. P. Wagner, I. Gordon, L. Trappeniers, J. Vanacken, F. Herlach, V.V. Moshchalkov, and Y. Bruynseraede, *Phys. Rev. Lett.* **81**, 3980 (1998).

22. Z.Q. Li, H. Liu, Y.H. Cheng, W.B. Mi, A. Yu, H.L. Bai, and E.I. Jiang, *Physica* **B353**, 324 (2004).

23. P.W. Kolb, D.B. Romero, H.D. Drew, Y. Moritomo, A.B. Souchkov, and S.B. Ogale, *Phys. Rev.* **B70**, 224415 (2004).

24. V. Eremenko, S. Gnatchenko, N. Makedonska, Yu. Shabakayeva, M. Shvedun, V. Sirenko, J. Fink-Finowicki, K.V. Kamenev, G. Balakrishnan, and D. McK Paul, *Fiz. Nizk. Temp.* **27**, 1258 (2001) [*Low Temp. Phys.* **27**, 930 (2001)].

25. Y.H. Hyun, J.S. Park, T.W. Eom, G.H. Kim, Y.S. Lee, Y.P. Lee, V.G. Prokhorov, and V.L. Svetchnikov, *Appl. Phys. Lett.* **93**, 042515 (2008).

26. A.J. Millis, T. Darling, and A. Migliori, *J. Appl. Phys.* **83**, 1588 (1998).

27. V.G. Prokhorov, V.A. Komashko, G.G. Kaminsky, K.K. Yu, S.J. Jun, S.Y. Park, J.S. Park, Y.P. Lee, and V.L. Svetchnikov, *Fiz. Nizk. Temp.* **33**, 78 (2007) [*Low Temp. Phys.* **33**, 58 (2007)].

28. Y.P. Lee, S.Y. Park, Y.H. Hyun, J.B. Kim, V.G. Prokhorov, V.A. Komashko, and V.L. Svetchnikov, *Phys. Rev.* **B73**, 224413 (2006).

29. I.O. Shklyarevskiy, M.Yu. Shvedun, S.L. Gnatchenko, P.J.M. van Bentum, P.C. Cristianen, J.C. Maan, and K.V. Kamenev, *Fiz. Nizk. Temp.* **27**, 1250 (2001) [*Low Temp. Phys.* **27**, 923 (2001)].

30. F. Rivadulla, M.A. Lypez-Quitela, and J. Rivas, *Phys. Rev. Lett.* **93**, 167206 (2004).

31. J.R.L. de Almaida and D.J. Thouless, *J. Phys.* **A11**, 983 (1978).

32. D.S. Fisher and D.A. Huse, *Phys. Rev.* **B38**, 373 (1988).

33. L. Néel, *C.R. Acad. Sci. URSS* **228**, 664 (1949).

34. W.F. Brown, *Phys. Rev.* **130**, 1677 (1963).

35. R.W. Chantrell and P. Wohlfarth, *Phys. Status Solidi* **A91**, 619 (1985).

36. R. Skomski, *J. Phys.: Condens. Matter* **15**, 841 (2003).

37. J. Du, B. Zhang, R.K. Zheng, and X.X. Zhang, *Phys. Rev.* **B75**, 014415 (2007).

38. P. Allia, M. Coisson, P. Tiberto, F. Vinai, M. Knobel, M.A. Novak, and W.C. Nunes, *Phys. Rev.* **B64**, 144420 (2001).

39. O. Margeat, M. Tran, M. Spasova, and M. Farle, *Phys. Rev.* **B75**, 134410 (2007).

40. P. Allia, F. Celegato, M. Coisson, A. Da Re, F. Ronconi, F. Spizzo, P. Tiberto, and F. Vinai, *J. Magn. Magn. Mater.* **290–291**, 580 (2005).